Monthly Notices
of the
ROYAL ASTRONOMICAL SOCIETY

Mon. Not. R. Astron. Soc. **427,** 1209–1218 (2012) doi:10.1111/j.1365-2966.2012.22049.x

Herschel⋆-ATLAS: the far-infrared properties and star formation rates of broad absorption line quasi-stellar objects

J. M. Cao Orjales,[1]† J. A. Stevens,[1] M. J. Jarvis,[1,2] D. J. B. Smith,[1] M. J. Hardcastle,[1] R. Auld,[3] M. Baes,[4] A. Cava,[5] D. L. Clements,[6] A. Cooray,[7] K. Coppin,[8] A. Dariush,[6] G. De Zotti,[9,10] L. Dunne,[11] S. Dye,[12] S. Eales,[3] R. Hopwood,[6,13] C. Hoyos,[12] E. Ibar,[14] R. J. Ivison,[14,15] S. Maddox,[11] M. J. Page[16] and E. Valiante[3]

[1]*Centre for Astrophysics Research, Science & Technology Research Institute, University of Hertfordshire, Hatfield AL10 9AB*
[2]*Physics Department, University of the Western Cape, Cape Town 7535, South Africa*
[3]*School of Physics and Astronomy, Cardiff University, The Parade, Cardiff CF24 3AA*
[4]*Sterrenkundig Observatorium, Universiteit Gent, Krijgslaan 281 S9, B-9000 Gent, Belgium*
[5]*Departamento de Astrofísica, Facultad de CC. Físicas, Universidad Complutense de Madrid, E-28040 Madrid, Spain*
[6]*Department of Physics, Imperial College London, Prince Consort Road, London SW7 2AZ*
[7]*Department of Physics and Astronomy, University of California, Irvine, CA 92697, USA*
[8]*Department of Physics, McGill University, 3600 rue University, Montréal, Québec, PQ H3A 2T8, Canada*
[9]*INAF-Osservatorio Astronomico di Padova, Vicolo dell'Osservatorio 5, I-35122 Padova, Italy*
[10]*SISSA, Via Bonomea 265, I-34136 Trieste, Italy*
[11]*Department of Physics and Astronomy, University of Canterbury, Private Bag 4800, Christchurch 8140, New Zealand*
[12]*School of Physics and Astronomy, University of Nottingham, University Park, Nottingham NG7 2RD*
[13]*Department of Physical Sciences, The Open University, Milton Keynes MK7 6AA*
[14]*UK Astronomy Technology Centre, Science and Technology Facilities Council, Royal Observatory, Blackford Hill, Edinburgh EH9 3HJ*
[15]*Institute for Astronomy, University of Edinburgh, Blackford Hill, Edinburgh EH9 3HJ*
[16]*Mullard Space Science Laboratory, University College London, Holmbury St. Mary, Dorking, Surrey RH5 6NT*

Accepted 2012 September 4. Received 2012 September 3; in original form 2012 May 10

ABSTRACT

We have used data from the *Herschel* Astrophysical Terahertz Large-Area Survey (H-ATLAS) at 250, 350 and 500 μm to determine the far-infrared (FIR) properties of 50 broad absorption line quasars (BAL QSOs). Our sample contains 49 high-ionization BAL QSOs (HiBALs) and one low-ionization BAL QSO (LoBAL) which are compared against a sample of 329 non-BAL QSOs. These samples are matched over the redshift range $1.5 \leq z < 2.3$ and in absolute *i*-band magnitude over the range $-28 \leq M_i \leq -24$. Of these, three BAL QSOs (HiBALs) and 27 non-BAL QSOs are detected at the $>5\,\sigma$ level. We calculate star formation rates (SFRs) for our individually detected HiBAL QSOs and the non-detected LoBAL QSO as well as average SFRs for the BAL and non-BAL QSO samples based on stacking the *Herschel* data. We find no difference between the HiBAL and non-BAL QSO samples in the FIR, even when separated based on differing BAL QSO classifications. Using Mrk 231 as a template, the weighted mean SFR is estimated to be $\approx 240 \pm 21\,\mathrm{M}_\odot\,\mathrm{yr}^{-1}$ for the full sample, although this figure should be treated as an upper limit if active galactic nucleus (AGN)-heated dust makes a contribution to the FIR emission. Despite tentative claims in the literature, we do not find a dependence of C IV equivalent width on FIR emission, suggesting that the strength of any outflow in these objects is not linked to their FIR output. These results strongly suggest that BAL QSOs (more specifically HiBALs) can be accommodated within a simple AGN unified scheme in which our line of sight to the nucleus intersects outflowing material. Models in which HiBALs are

⋆The *Herschel*-ATLAS is a project with *Herschel*, which is an ESA space observatory with science instruments provided by European-led Principal Investigator consortia and with important participation from NASA. The H-ATLAS website is http://www/h-atlas.org/.
†E-mail: jc10acd@herts.ac.uk

caught towards the end of a period of enhanced spheroid and black hole growth, during which a wind terminates the star formation activity, are not supported by the observed FIR properties.

Key words: galaxies: active – galaxies: photometry – quasars: absorption lines.

1 INTRODUCTION

Mergers and other interactions are thought to trigger active galactic nucleus (AGN) which can lead to outflows that affect the chemical make-up of the interstellar and intergalactic media, and limit star formation in the host galaxy (Bower et al. 2006; Croton et al. 2006; De Lucia & Blaizot 2007; Booth & Schaye 2009) and possibly in the large-scale environment (Rawlings & Jarvis 2004; McCarthy et al. 2010). The role of these outflows has become an important feature of contemporary models of the formation and evolution of galaxies over cosmic time, being required in theoretical attempts to understand galaxy 'downsizing' (Cowie et al. 1996; Scannapieco, Silk & Bouwens 2005). In semi-analytic models of galaxy assembly (Granato et al. 2004) AGN feedback removes dense gas from the centres of galaxies, heating up the surrounding intergalactic medium (IGM), while at the same time enriching the IGM with metals. Studies such as that of Gabel, Arav & Kim (2006) indicate that outflows have high metallicities which could serve to enrich the IGM. Due to the IGM's low density, however, it cannot cool efficiently and so cannot fall back to the galaxy to fuel star formation.

Simulations of galaxy mergers (Springel, Di Matteo & Hernquist 2005) show that AGN feedback can heat the interstellar medium (ISM) and inhibits star formation, with outflows providing the energy and momentum feedback for the ISM of the host galaxy. Efforts to include these mechanisms (e.g. Croton et al. 2006; Sijacki et al. 2007) have focused on two modes: a 'radio mode' whereby a relativistic jet can heat interstellar gas and intracluster media, stopping further infall of mass (Best 2007; Best & Heckman 2012), and a 'quasar mode', which serves to stop star formation with an outflow of greater mass but with a lower velocity driven by the radiation from the quasar. At the same time, the quasar mode removes any leftover gas that might serve to enshroud the galaxy, turning it into a 'classical' quasi-stellar object (QSO). Recent work finds that when feedback is incorporated, the Λ cold dark matter model provides a good fit to observed galaxy stellar-mass fractions and the K-band luminosity function (Bower et al. 2006; Cirasuolo et al 2010). However, if feedback is excluded in galaxy group simulations, the temperature profiles are highly peaked and in disagreement with many of the observed properties of galaxies. The simulations also suffer from the well-known overcooling problem, the resulting stellar-mass fraction being several times larger than observed (McCarthy et al. 2010).

Gas outflows from AGN are primarily detected in X-ray and ultraviolet absorption against the inner portions of the accretion disc and/or the more extended broad-line region. Indicators for the origin of an absorption line system are (1) velocity width, (2) partial coverage, (3) time variability and (4) high metallicity. Historically, the criterion of velocity width has led to the use of three categories of intrinsic absorbers. Those with the greatest velocity dispersions are termed 'broad absorption line' quasars (BAL QSOs; e.g. Weymann et al. 1991). These have absorption lines with full width at half-maximum (FWHM) greater than 2000 km s^{-1}. Those with very narrow absorption lines are known as 'narrow absorption line' QSOs, (NAL QSOs; e.g. Hamann & Ferland 1999). These have FWHM of less than 500 km s^{-1}. Finally, the last type are known as mini-BALs. These are those intrinsic absorbers whose velocity widths are between 500 and 2000 km s^{-1} (e.g. Hamann et al. 1997; Churchill et al. 1999).

There is still some debate in the literature regarding BAL QSOs, with the observed fraction ($\sim$15 per cent) being attributed to orientation, an evolutionary phase or some mixture of both. In the orientation hypothesis, BAL outflows are present in all QSOs but they are only viewed as BAL QSOs when our line of sight intersects the solid angle subtended by the BAL outflow. In this situation, high column density accretion disc winds are accelerated by radiation pressure (Murray et al. 1995; Murray & Chiang 1998; Elvis 2000). This model attributes the fraction of QSOs to the fractional solid angle coverage of the BAL regions. Furthermore, it is able to account for the similarity of the continua and emission-line features in BAL QSO and non-BAL QSO spectra once reddening is taken into account (Weymann et al. 1991; Reichard et al. 2003a) and fits well with unified models (Antonucci 1993; Elvis et al. 1994; Elvis 2000). Mid-infrared (mid-IR) and far-infrared (FIR) studies also show no difference in emission, consistent with there being similar dust masses within the host galaxy and BAL QSOs being an orientation effect (Gallagher et al. 2007; Lazarova et al. 2012). However, spectropolarimetry studies (Ogle et al. 1999; DiPompeo et al. 2010, 2011) indicate that BAL QSOs are seen at a wide range of inclinations, which suggests that BAL QSOs may not be just a simple orientation effect.

The evolutionary scenario is rather different. In such a model, BAL QSOs are young QSOs that may have recently undergone a merger/starburst, and are observed as BAL QSOs when two special conditions are met; first, the QSO luminosity has reached a sufficient strength to accelerate gas to several thousand km s^{-1} and secondly, there is a large mass of diffuse gas and dust in the nuclear regions leading to a rapid mass-loss phase. These BAL outflows could also play a role in terminating star formation and removing much of the obscuring dust and gas leading to a classical optically and soft X-ray luminous QSO (Voit, Weymann & Korista 1993; Hall et al. 2002; Page et al. 2004, 2011). If BAL QSOs are caught towards the end of an epoch of enhanced star formation activity, then high dust masses within the host galaxies of BAL QSOs will yield higher average FIR flux densities. Since FIR emission is optically thin, there should be no dependence on the source orientation. This difference in the FIR properties in these two hypotheses can in principle be used to distinguish between them.

Omont et al. (1996) and Carilli et al. (2001), both working at frequencies around 250 GHz, showed that there was weak evidence that BAL QSOs were more luminous at millimetre wavelengths than ordinary QSOs. This would favour an evolutionary scenario, but the work did not concentrate exclusively on the BAL QSO phenomenon, or compare star formation rates (SFRs), and the samples were small (four and seven BAL QSOs, respectively). Other work by Lewis, Chapman & Kuncic (2003), Willott, Rawlings & Grimes (2003) and Priddey et al. (2007) was specifically aimed at improving our understanding of the BAL phenomenon, with larger samples of 7, 30 (41 non-BAL QSOs for a comparison sample) and 15 BAL QSOs (supplemented by data from Priddey et al. 2003), respectively. All of these samples were observed using the Submillimetre

Common User Bolometer Array (SCUBA) camera on the James Clerk Maxwell Telescope at wavelengths of 450 and 850 μm. The samples of Willott et al. (2003) and Priddey et al. (2007) are composites of previous work by the authors at FIR wavelengths, and therefore have non-uniform sensitivity coverage. None of these studies finds strong evidence for BAL QSOs to be more submillimetre (submm) luminous than non-BAL QSOs, a finding consistent with the orientation model for BAL activity. Within the BAL QSO population itself, however, Priddey et al. (2007) find tentative evidence for a dependence of submm emission on C IV absorption-line equivalent width and discuss the implications within the framework of simple evolutionary models.

In this paper, we use *Herschel* (Pilbratt et al. 2010) data to study the FIR properties of matched samples of BAL and non-BAL QSOs allowing us to build on previous work with improved statistics, better wavelength coverage around the FIR dust peak and better matching of the control sample. Throughout this work, we use a cosmology where $H_0 = 70\,\mathrm{km\,s^{-1}\,Mpc^{-1}}$, $\Omega_\mathrm{m} = 0.3$ and $\Omega_\Lambda = 0.7$.

2 THE DEFINITION OF A BAL QSO

BAL QSOs have BALs which arise from resonance line absorption in gas outflowing with velocities up to $0.1c$ (Weymann et al. 1991; Arav et al. 2001; Hall et al. 2002; Reichard et al. 2003a). As a subclass of AGN, BALs until recently were thought to make up around 10−15 per cent of the sources in QSO surveys (Weymann et al. 1991; Tolea, Krolik & Tsvetanov 2002; Reichard et al. 2003a). However, Trump et al. (2006) quoted a much higher BAL fraction, i.e. an observed fraction within the third Data Release (DR3) of the Sloan Digital Sky Survey (SDSS; Schneider et al. 2005) of 26 per cent. It is possible that selection effects may bias us against BAL identifications, meaning that the intrinsic fraction is far higher than observed (Hewett & Foltz 2003; Dai, Shankar & Sivakoff 2008). Perhaps the most widely accepted classification scheme for whether a QSO is a BAL QSO is the balnicity index (BI), defined by Weymann et al. (1991),

$$\mathrm{BI} = \int_{3000}^{25\,000} \left[1 - \frac{f(-v)}{0.9}\right] C\,\mathrm{d}v. \quad (1)$$

Here, $f(v)$ is the continuum-normalized spectral flux at a velocity v (in $\mathrm{km\,s^{-1}}$) from the C IV line rest wavelength of 1549 Å (in the system frame). The dimensionless value C is 0 unless the observed spectrum has fallen at least 10 per cent below the continuum for a velocity width of at least $2000\,\mathrm{km\,s^{-1}}$ in the absorption trough, at which point C is set to 1. Traditional BALs are defined to have $\mathrm{BI} > 0$.

We construct our BAL sample using BAL QSOs selected using the BI metric of equation (1) and a version of the metric which is 'extended' as in Gibson et al. (2009a), the lower limit of the BI being $0\,\mathrm{km\,s^{-1}}$.

BAL QSOs can be split into subclasses based on their observed spectral features. The first of these classifications are high-ionization BAL QSOs (HiBALs). These objects contain absorption in Ly α λ1216 Å, N V λ1240 Å, Si IV λ1394 Å and C IV λ1549 Å. They are the most prevalent subpopulation, making up around 85 per cent of BALs. The low ionization BAL QSO (LoBALs) contain all of the previously mentioned absorption features seen in HiBALs, but also contain absorption features in Mg II λ2799 Å and other low-ionization species. These objects comprise around 15 per cent of BALs (Sprayberry & Foltz 1992 estimated 17 per cent). HiBALs and LoBALs are found to have redder continua than non-BALs (Brotherton et al. 2001; Reichard et al. 2003b; Scaringi et al. 2009), with LoBALs also being significantly redder than HiBALs (Weymann et al. 1991; Sprayberry & Foltz 1992). The third and final class are FeLoBALs, which show the absorption features of LoBALs as well as absorption features arising from metastable excited levels of iron. The effects of these definitions on each measured variable are discussed in greater detail in Section 4.

3 DATA AND SAMPLE SELECTION

The BAL QSO sample that we use in this paper is a small proportion of those objects identified as a BAL QSO within the SDSS QSO catalogue (Gibson et al. 2009a), which number 5039 BAL QSOs. By using the SDSS catalogue (both for BAL and non-BAL samples) a redshift of $z < 2.3$ provides an upper redshift limit where the SDSS colour selection criteria are relatively unaffected by BAL absorption (Gibson et al. 2009a). We use absolute magnitude in the SDSS i band since it is less affected by dust reddening than the bluer bands.

As Gibson et al. (2009a) used the BI as a classification mechanism, it is possible that some BALs will have been missed from the sample, and others included within the catalogue will be misclassifications (though the strictness of the BI should decrease the number).

In this paper, we use observations from the ESA *Herschel Space Observatory* (Pilbratt et al. 2010) as part of the *Herschel* Astrophysical Terahertz Large-Area Survey (H-ATLAS; Eales et al. 2010) survey phase 1 data set, reduced in the same way as the Science Demonstration Phase (SDP) data set and with the same 5σ flux limits (Ibar et al. 2010; Pascale et al. 2011; Rigby et al. 2011). It is the largest *Herschel* open-time extragalactic key project on the observatory, and will eventually observe $\sim 550\,\mathrm{deg^2}$ in five passbands at 100, 160, 250, 350 and 500 μm with the Photodetecting Array Camera and Spectrometer (PACS) (Poglitsch et al. 2010) and the Spectral and Photometric Imaging Receiver (SPIRE) (Griffin et al. 2010) instruments, allowing the study of interstellar dust at angular scales $\simeq$10 times smaller than with *IRAS*. With these data, approximately 250 000 galaxies out to redshifts of three to four are expected to be detected. We omit the PACS data (Ibar et al. 2010) from our analysis as the selected sources may possibly be contaminated by warmer dust heated by the AGN and the data do not reach the required depth to be useful. Instead, we have concentrated on the SPIRE data (Pascale et al. 2011). SPIRE wavelengths have been chosen because they are less likely to be contaminated by direct emission from the warm dust of the AGN torus, with a starburst component at these wavelengths being required to account for the total FIR emission, as suggested by the spectral energy distribution (SED) fits of Hatziminaoglou et al. (2010).

The Gibson et al. (2009a) catalogue has been cross-matched with the H-ATLAS 9-, 12- and 15-h fields. Each field is approximately 12° in RA by 3° in Dec. (6° by 3° for the 12-h field), which places a limit on the size of our final sample. Only those QSOs falling within the field boundaries are included resulting in an initial sample of 88. These further reduce to 83 due to five that have a C IV BI value of 0. These BAL QSOs have been classified using alternative lines such as Si IV or Mg II, and are considered beyond the scope of this paper.

We next apply constraints within the parameter space $1.5 \leq z < 2.3$ and $-28 \leq M_\mathrm{i} \leq -24$, where most of the BAL QSOs lie, in order to reduce the susceptibility of our study to the effects of luminosity or redshift evolution (e.g. Bonfield et al. 2011). This restriction gives two advantages: it allows easy construction of a

non-BAL QSO comparison sample and limits the effects of cosmological evolution whilst comparing similar luminosities. In this way the sample is further reduced to 50 BAL QSOs. We have also addressed the important distinction between the 'classic' BI and the 'extended' version given in Gibson et al. (2009a), BI_0, to see if this classification has any effect on the flux densities and other properties of our sample. As a result of this distinction, the total number of BAL QSOs following the 'classic' BI definition drops to 36. One of these, SDSS115404.13+001419.6, is a LoBAL QSO. This source is not considered in our stacking analyses in Section 4. The distribution of BAL QSOs over the three fields is as follows – 9-h field: 19; 12-h field: 12; and 15-h field: 19. Our comparison sample consists of 329 non-BAL QSOs drawn from the SDSS DR5 (Schneider et al. 2007). We did not use the SDSS DR8 catalogue since there has been no corresponding BAL QSO catalogue produced. We trimmed objects at random from overpopulated parts of the comparison sample (determined via visual inspection of M_i and z) until a two-sample Kolmogorov–Smirnov (KS) test comparison in M_i and z between the non-BAL and BAL QSO samples returned a null-hypothesis probability of $p > 0.05$; for the final non-BAL QSO comparison sample separate KS tests on redshift and M_i give p-values of 0.67 and 0.20, respectively ('extended sample') and 0.89 and 0.17, respectively ('classic' sample). Running a 2-d KS test (Peacock 1983) on redshift and M_i for both samples returns a p-value of 0.27. We can therefore assume that the populations are adequately matched in M_i and z. The lower panel of Fig. 1 shows the final BAL and non-BAL QSO samples on the (z, M_i) plane, while Table 1 gives details of the final BAL QSO sample.

In the next section, we compare the FIR properties of matched BAL and non-BAL QSO samples, and determine SFRs for the samples based on separate classification schemes (as explained in Section 2). Our study improves on previous work since whilst the H-ATLAS survey is still not complete, the three fields in the H-ATLAS phase 1 data set centred at 9, 12, and 15 h give us a large area providing a uniformly selected sample of objects cross-matched with the SDSS.

4 METHOD AND RESULTS

Here we determine the FIR properties of the selected QSOs and investigate how the BAL QSOs relate to the non-BAL QSOs. We further discuss the effects of different selection criteria, i.e. BI versus BI_0.

4.1 Stacking analysis

The FIR flux densities used in this section are taken directly from the final point spread function (PSF)-convolved images for all three H-ATLAS fields. Cutouts of set size (210×210 arcsec^2) of the region surrounding each BAL/non-BAL QSO are generated, and these are co-added, each pixel being the weighted mean flux density in that pixel. The weighted mean stacked flux density value of each source is taken to be that at the centre of the stacked image which is the closest pixel to the catalogue position in either the Gibson et al. (2009a) BAL or Schneider et al. (2007) SDSS QSO samples. We background subtract by randomly selecting a sample of 40 000 pixel from each field to create a mean background for that field at that wavelength. We then subtract this mean background from every pixel in our cutout images for each QSO. These mean values for each wavelength are shown in Table 2, while Fig. 2 shows the BAL and non-BAL QSO stacked images at each wavelength.

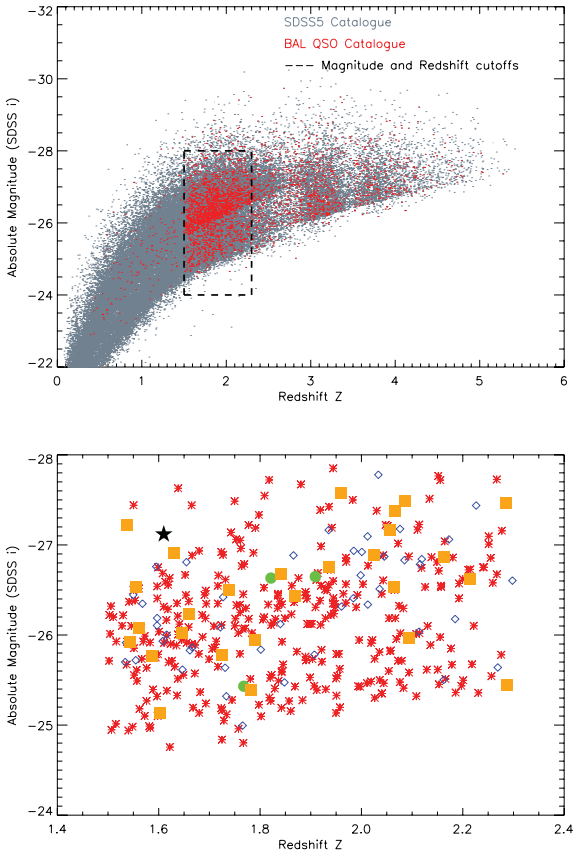

Figure 1. Distributions of BAL and non-BAL QSOs as a function of redshift and absolute magnitude in SDSS i band. The top panel shows the full sample before our selection methods have been used. The dashed box shows the redshift and absolute magnitude cut-offs used in this study. The lower panel shows the final sample after removal of those QSOs falling outside our absolute magnitude and redshift cut-offs, and after statistical matching (see text for details). Red asterisks are non-BAL QSOs, blue diamonds are HiBAL QSOs, the black filled star is our solitary LoBAL QSO, green circles are our detected HiBAL QSOs and orange squares are our detected non-BAL QSOs.

We find that at longer wavelengths the stacked BAL QSO image is less distinguishable from the background, which is expected due to increased confusion noise and a higher instrumental noise; galaxies at 500 μm are also expected to be fainter, since the Rayleigh–Jeans tail is being sampled. Table 2 shows the central pixel values of the stacks. We find that there is no statistical difference between BAL QSOs and non-BAL QSOs; their flux densities in all bandpasses are the same within the errors. This result holds for both the 'classic' and 'extended' BAL QSO samples.

We attempt to reproduce our results using the Institut d'Astrophysique Spatiale (IAS) stacking library. It stacks data to allow a statistical detection of a faint signal using positions of galaxies detected at shorter wavelengths as with our method but has also been tested and validated with galaxy clustering in mind, something which may affect our results (see Bavouzet 2008; Bethermin et al. 2010 for further details). However, we still find no difference between the BAL QSO and non-BAL QSO samples in each bandpass and the IAS values are in agreement with our values within the errors (see Table 2).

It should be noted that submm fluxes may still be overestimated due to clustering of sources if they emit in the SPIRE bands, but since we cannot identify the sources around the QSO at high

Table 1. The BAL QSO Sample. The classification method used to determine the Balnicity of a source is given in the type/detected column, along with whether it is detected. If a source is classified using BI, then it will also be classified as a BAL QSO by the BI_0 definition. The 250 μm flux density and signal-to–noise ratio are given derived from the 250 μm flux density divided by the sum in quadrature of the instrumental noise in the corresponding pixel and confusion noise in Rigby et al. (2011). 5σ detections found in the phase 1 catalogue with matched optical/NIR counterparts (see Section 4.2) are shown with their flux density values taken from the phase 1 catalogue. The average 5σ limits at 250, 350 and 500 μm are 33.5, 37.7 and 44.0 mJy beam^{-1}. For undetected sources, their flux density values are the best estimates from measuring the flux density in the closest pixel of the PSF-smoothed map and noise map and are not reliably associated with $R > 0.80$ to a 250 μm source as for our detections. The FIR data for the non-BAL quasars within H-ATLAS will be dealt with in a future paper (Bonfield et al., in preparation), however all maps and catalogues used in this paper will be released as part of the phase 1 data release from the H-ATLAS website.

Source	z	Type/ detected?	C IV EW (Å)	M_i	250 μm flux density (mJy)	S/N 250	350 μm flux density (mJy)	S/N 350	500 μm flux density (mJy)	S/N 500
SDSSJ084307.36−001228.4	1.7271	**BI/no**	7.40	−26.421	+18.43	+2.82	+13.44	+1.86	+6.00	+0.75
SDSSJ084524.10−000915.4	2.0121	**BI/no**	56.10	−27.095	+18.38	+3.18	+2.79	+0.41	+2.67	+7.84
SDSSJ084842.13+010044.3	1.6616	**BI/no**	20.00	−25.830	−4.13	−0.63	−3.79	−0.52	−4.00	−0.047
SDSSJ085316.22+012052.0	1.6663	**BI/no**	19.80	−25.862	+13.58	+2.11	+12.29	+1.68	+3.83	+0.44
SDSSJ085436.41+022023.5	1.9089	**BI/yes**	20.70	−26.648	+55.87	+8.24	+63.14	+7.90	+39.87	+4.51
SDSSJ085609.02+001357.7	1.8401	**BI/no**	6.50	−26.122	+9.74	+1.51	+6.88	+0.94	−1.72	−0.21
SDSSJ085647.99+003107.4	2.2979	**BI/no**	8.70	−26.604	+21.94	+3.45	+15.61	+2.15	+20.58	+2.39
SDSSJ090030.36+015154.9	1.9848	**BI/no**	10.00	−26.935	−4.41	−0.67	−3.42	−0.46	−0.786	−0.09
SDSSJ090211.60+003859.5	1.5339	**BI/no**	7.60	−25.700	+16.06	+2.44	−1.30	+0.18	+0.08	+0.09
SDSSJ090331.90+011804.5	1.9072	**BI/no**	17.60	−25.782	+11.88	+1.85	+3.48	+0.47	+10.01	+1.18
SDSSJ090517.24+013551.4	1.7678	**BI/yes**	41.70	−25.431	+57.81	+8.54	+72.79	+8.97	+52.59	+5.86
SDSSJ090523.07+001136.9	1.5600	**BI/no**	8.20	−26.348	+22.02	+3.44	+19.48	+2.74	+7.55	+0.90
SDSSJ090904.52−000234.5	1.7656	**BI_0/no**	8.50	−24.995	−3.85	−0.59	−10.09	−1.39	−2.88	−0.33
SDSSJ091110.29+004822.8	2.2691	**BI_0/no**	4.00	−25.640	+3.85	+0.66	+4.19	+0.63	+2.94	+0.38
SDSSJ091144.41+000423.6	1.8014	**BI_0/no**	5.70	−25.838	+3.08	+0.53	+0.23	+0.03	+4.79	+0.62
SDSSJ091524.29+002032.6	1.9353	**BI_0/no**	6.00	−27.165	+23.22	+3.56	+15.38	+2.12	+8.98	+1.06
SDSSJ091600.60+011621.6	1.8481	**BI/no**	15.20	−25.474	+3.08	+0.47	−3.40	−0.47	−5.01	−0.57
SDSSJ091808.80+005457.7	2.1155	**BI/no**	5.30	−26.785	+3.73	+0.56	−0.65	−0.08	−3.37	−0.39
SDSSJ091951.29+005854.9	2.1138	**BI/no**	6.90	−26.037	+4.62	+0.70	+7.60	+1.04	+9.19	+1.05
SDSSJ113510.27−003558.2	1.7335	**BI/no**	8.30	−25.320	+8.17	+1.25	−12.53	−1.75	−2.66	−0.31
SDSSJ113537.56+004130.1	1.5498	**BI/no**	15.00	−26.445	+4.52	+0.69	−6.21	−0.84	+0.83	+0.01
SDSSJ113544.33+001118.7	1.7311	**BI/no**	23.80	−25.637	−0.35	−0.05	+2.62	+0.36	+0.72	+0.08
SDSSJ113651.54−002836.0	1.6157	**BI/no**	7.50	−26.004	+12.83	+1.95	+7.51	+1.05	+10.93	+1.28
SDSSJ113934.63−005901.5	1.6079	**BI/no**	10.40	−25.932	+9.06	+1.39	+2.61	+0.35	−0.8	−0.092
SDSSJ114259.29−000156.4	1.9840	**BI_0/no**	9.30	−26.408	−3.91	−0.59	−2.86	−0.39	+11.61	+1.38
SDSSJ114333.62+013709.0	1.5547	**BI/no**	22.70	−25.720	+21.98	+3.36	+29.35	+3.97	−4.46	−0.53
SDSSJ114954.94+001255.3	1.5952	**BI/no**	4.90	−26.759	+11.45	+1.75	+14.51	+2.01	+19.20	+2.23
SDSSJ115404.13+001419.6	1.6100	**BI/no**	31.50	−27.119	+29.88	+4.49	+20.68	+2.86	−0.24	−0.03
SDSSJ115407.74+001113.4	1.6547	**BI_0/no**	7.90	−26.809	+32.72	+4.94	+38.02	+4.47	+38.02	+4.46
SDSSJ115809.69−013754.3	1.5969	**BI/no**	17.70	−26.188	−0.84	−0.13	+4.61	+0.64	−4.81	−0.57
SDSSJ115940.79−003203.5	2.0334	**BI_0/no**	5.70	−27.779	+28.25	+4.36	+31.52	+4.26	+37.79	+4.38
SDSSJ140842.75+010828.7	1.6469	**BI/no**	15.80	−25.616	+2.45	+0.37	+5.23	+0.73	−1.87	−0.22
SDSSJ140918.72+004824.3	2.0008	**BI/no**	10.10	−26.922	+21.47	+3.32	+6.88	+0.96	+7.65	+0.89
SDSSJ141434.39−011534.4	1.5967	**BI_0/no**	13.70	−26.106	+12.73	+2.00	+10.06	+1.39	+15.00	+1.73
SDSSJ142050.33−002553.1	2.0850	**BI/no**	35.20	−26.831	+10.18	+1.76	+2.62	+0.39	−10.75	−1.37
SDSSJ142423.76+001451.0	2.1849	**BI_0/no**	10.30	−26.177	−2.54	−0.39	+7.44	+1.03	+0.59	+0.06
SDSSJ142820.59−005348.3	1.5357	**BI_0/no**	5.30	−25.914	+23.56	+3.63	+24.28	+3.37	−5.39	−0.64
SDSSJ143030.97+003440.1	1.9985	**BI_0/no**	14.40	−26.663	+9.03	+1.56	+3.67	+0.56	−3.08	−0.40
SDSSJ143144.65+011644.1	1.9607	**BI/no**	20.50	−26.316	+6.50	+1.02	+10.24	+1.41	+5.51	+0.66
SDSSJ143209.79+015256.3	2.1191	**BI/no**	23.20	−26.842	+16.09	+2.51	+12.22	+1.69	+6.43	+0.76
SDSSJ143627.79+004655.7	2.1625	**BI_0/no**	7.90	−25.503	+16.87	+2.64	+1.24	+0.17	+2.83	+0.33
SDSSJ143641.24+001558.9	1.8659	**BI/no**	20.80	−26.884	+3.13	+0.49	−7.55	−1.03	−11.05	−1.27
SDSSJ143758.06+011119.5	2.0450	**BI/no**	18.80	−26.871	+3.56	+0.59	+12.90	+1.89	+5.59	+0.69
SDSSJ143907.51−010616.7	1.8214	**BI_0/yes**	7.60	−26.632	+73.35	+10.55	+42.41	+5.34	+29.32	+3.31
SDSSJ144256.86−004501.0	2.2264	**BI/no**	2.50	−27.438	+9.88	+1.71	+19.66	+2.96	+18.44	+2.36
SDSSJ144434.80+003305.3	2.0359	**BI_0/no**	7.60	−26.511	+8.44	+1.43	−2.70	−0.40	−5.33	− 0.67
SDSSJ144911.82−010014.8	2.1728	**BI/no**	39.60	−27.061	+4.12	+0.64	+0.29	+0.04	+3.75	+0.49
SDSSJ144959.96+003225.3	1.7217	**BI/no**	11.00	−26.085	+11.90	+1.87	+1.18	+0.16	−4.06	−0.48
SDSSJ145045.42−004400.3	2.0762	**BI/no**	18.00	−27.178	+10.38	+1.60	−1.79	−0.24	−0.68	−0.08
SDSSJ145511.44+002146.0	2.0126	**BI/no**	15.80	−26.338	+0.61	+0.09	−2.44	−0.34	+3.80	+0.45

Table 2. The BAL ('extended' and 'classic' samples) and non-BAL QSO FIR weighted mean flux densities in the 250, 350 and 500 μm bandpasses. The number in brackets gives the number of objects within each stack. We also include here our determined background noise for each field at each wavelength.

	BAL QSO and non-BAL QSO flux densities			IAS BAL QSO and non-BAL QSO flux densities			Mean background in each field		
Bandpass (μm)	'Extended' stack (49, mJy)	'Classic' stack (35, mJy)	non-BAL stack (329, mJy)	'Extended' stack (49, mJy)	'Classic' stack (35, mJy)	non-BAL stack (329, mJy)	9-h field (mJy)	12-h field (mJy)	15-h field (mJy)
250	11.81 ± 1.20	10.97 ± 1.51	10.94 ± 0.53	12.34 ± 1.41	10.87 ± 1.61	11.74 ± 0.63	1.14 ± 0.0003	0.91 ± 0.0003	1.45 ± 0.0004
350	8.76 ± 1.52	8.13 ± 2.11	8.97 ± 0.42	10.80 ± 1.61	8.79 ± 1.79	9.57 ± 0.69	2.82 ± 0.0003	2.72 ± 0.0003	3.05 ± 0.0003
500	5.78 ± 1.66	4.55 ± 2.11	7.25 ± 0.54	7.72 ± 1.41	5.48 ± 1.86	7.85 ± 0.62	0.30 ± 0.0003	0.27 ± 0.0003	0.84 ± 0.0003

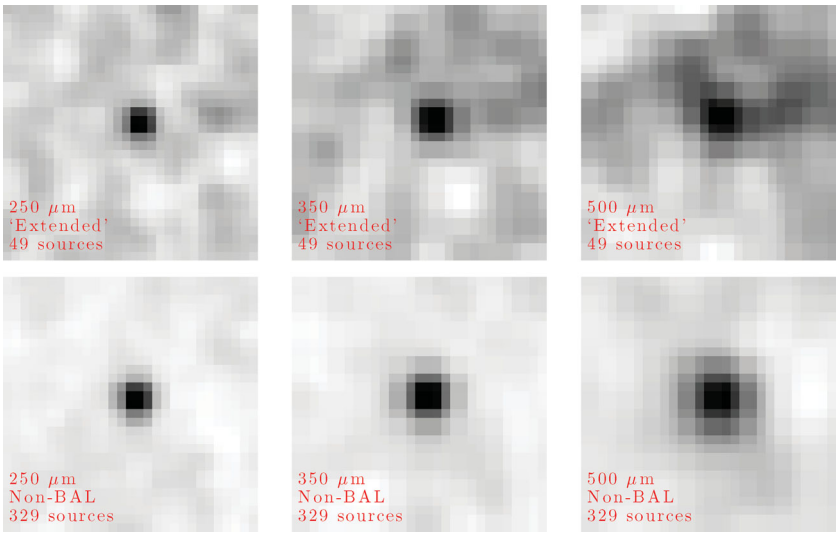

Figure 2. The 250, 350 and 500 μm weighted mean flux density stacks of the 'extended' BAL and non-BAL QSO (top and bottom rows, respectively) samples. Each postage stamp image is 210 × 210 arcsec^2. In each corner in red is given the wavelength, classification and the number of sources used to create that stack.

redshifts there is little that can be done to solve this problem. We also emphasize that the effects of confusion should be the same for both BAL QSOs and non-BAL QSOs since they are treated in an equal manner within both methods.

The Gaussian errors quoted in Table 2 must be treated with caution, since background noise will be non-Gaussian owing to confusion noise. To determine quantitatively whether the stacked BAL QSOs are detected significantly, flux densities from 120 000 randomly chosen positions in the field have been measured following Hardcastle et al. (2010). The random background compared with the BAL and non–BAL QSO fluxes is shown in Fig. 3. Using a KS test, we can examine whether the flux densities of the stacks are statistically distinguishable from those taken from randomly chosen positions, as a KS test is not influenced by the noise properties.

In comparison to the background we detect the BAL QSOs at all wavelengths using both classification schemes. The significance of the 250 μm detection for 'extended' BI_0 BAL QSOs is well over 5σ ($p < 10^{-10}$), and as expected, the significance decreases towards longer wavelengths, being lowest at 500 μm ($p \sim 5 \times 10^{-4}$). The larger sample of non-BAL QSOs is also detected with high significance above the background at all wavelengths ($p < 10^{-10}$). Returned KS probabilities are shown in Table 3. We also used a KS test to compare the distribution of flux densities between the BAL QSO samples and the non-BAL QSO samples (see Fig. 3). At 250, 350 and 500 μm, their p-values are $p = 0.39$, 0.80 and 0.37, respectively, for the 'extended' sample when comparing the BAL QSO sample with the full non-BAL QSO sample. We therefore cannot reject the null hypothesis that the BAL and non-BAL QSOs are drawn from the same underlying flux density distribution.

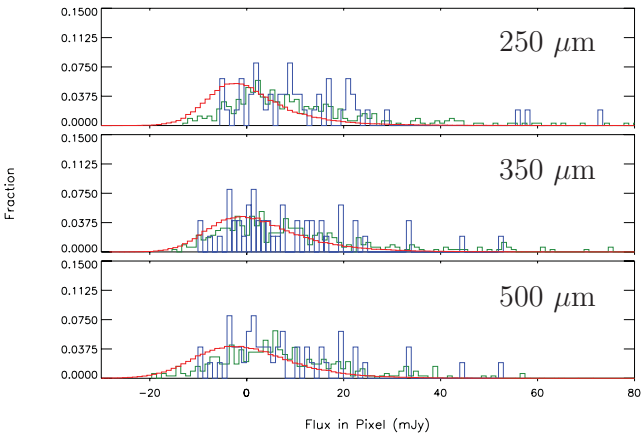

Figure 3. The distribution of flux density at each wavelength for the full BAL (blue outline) and non-BAL QSO (green outline) samples in bins of width 1 mJy. The random background flux densities are shown as a red outline.

We performed a second test where the 120 000 stacks were created from flux densities extracted from random positions, with the number of elements in the stack equal to the elements in the comparison sample stack, i.e. 49, 35 and 329, and we then compared these random stacks with the stacked flux densities of our BAL and non-BAL QSO samples. The fraction of random stacks where the

Table 3. The KS statistics and probabilities of each sample being indistinguishable from a randomly selected sample of flux densities taken from the H-ATLAS fields. The fraction shows how many random stacks had flux densities greater than our sample stacks.

	'Extended' BI_0			'Classic' BI			Non-BAL QSOs		
Bandpass (μm)	KS statistic	KS probability	Fraction	KS statistic	KS probability	Fraction	KS statistic	KS probability	Fraction
250	0.48	$<10^{-10}$	$<10^{-5}$	0.48	$<10^{-10}$	0.00013	0.38	$<10^{-10}$	$<10^{-5}$
350	0.32	$<10^{-10}$	0.00068	0.33	$<10^{-10}$	0.0028	0.29	$<10^{-10}$	$<10^{-5}$
500	0.28	0.00051	0.00048	0.29	0.0041	0.022	0.25	$<10^{-10}$	$<10^{-5}$

weighted mean flux density exceeds the weighted mean flux density in our sample stacks provides an estimate of the probability of the detection of our stacks being just a background fluctuation. We find that 250 μm is generally of greater significance than that at 500 μm for the BAL QSO samples (e.g. $p < 10^{-5}$ and $p = 4.8 \times 10^{-4}$, respectively, for the 'extended' BI_0 BAL QSOs in each bandpass), and that none of the 120 000 flux density stacks extracted at random positions has larger weighted mean flux densities than the BAL and non-BAL stacked flux densities as shown in Table 3. This indicates that our weighted mean flux density values in Table 2 are not due to background fluctuations.

4.2 Detection rates

We now investigate how many individual BAL QSOs are significantly detected in the H-ATLAS data at the $>5\sigma$ level. The phase 1 H-ATLAS catalogue used a likelihood ratio technique to identify optical and near-IR counterparts with objects detected by *Herschel* as with the SDP catalogue (Smith et al. 2011) in the phase 1 data. We find that three BAL QSOs from our sample are associated with (5σ) 250 μm sources in the H-ATLAS phase 1 catalogue (i.e. they have reliability, $R > 0.80$); two of these are 'classic' BI-defined BAL QSOs. For the non-BAL QSOs, 27 of the 329 have reliable $R > 0.80$ 250 μm counterparts. This raises the question of whether there is an actual difference in the detection rate of BAL QSOs and non-BAL QSOs. We detect 6.0 per cent of the 'extended' sample (8.3 per cent of the 'classic' BI-defined sample) compared to 8.2 per cent of the non-BAL sample. Comparing these detection rates using a binomial probability distribution gives a null result ($p = 0.19$ and 0.23 for the 'extended' and 'classic' samples, respectively). We cannot therefore reject the null hypothesis that the detected HiBALs are drawn from the same distribution as the detected non-BAL QSOs, consistent with our conclusions above on their flux density distribution.

4.3 FIR luminosities and star formation rates

We have limited information on the shape of the SED of our QSOs and therefore must choose a suitable template in order to compute FIR luminosities ($L_{\rm FIR}$). The primary galaxy that we have chosen for this purpose is Mrk 231. Of the local ultraluminous infrared galaxies (ULIRGs), it is the most luminous, with a rest-frame luminosity at 8–1000 μm of $3.2 \times 10^{12}\,L_\odot$ (Sanders et al. 2003), and it shows similar BAL features to our sample, having been classified as a BAL QSO, strictly a LoBAL QSO (Smith et al. 1995). We have also investigated the effect of using a template based on IZw1, a local Seyfert type 1 galaxy in the nearby Universe at $z = 0.0589$ (Ho & Kim 2009). We assume $T = 45$ K and emissivity index $\beta = 1.6$ for Mrk 231, and $T = 36$ K and $\beta = 1.7$ for IZw1 from fitting a greybody to data points retrieved from the NASA Extragalactic Database (32 and 9, respectively).

We determine the FIR luminosity via a ratio method between the 250 μm flux density of our greybody template if placed at the redshift of the QSO in our sample and the 250 μm flux density of the QSO. This implicitly assumes that the QSO has the same FIR SED as the greybody template. The calculation of the SFR was then performed in the standard manner using the relationship with $L_{\rm FIR}$ published by Kennicutt (1998) in equation (2) and these are presented in Table 4, i.e.

$$\mathrm{SFR}\ (\mathrm{M_\odot\ yr^{-1}}) = 4.5 \times 10^{-44} L_{\rm FIR}\ (\mathrm{ergs^{-1}}). \quad (2)$$

The Kennicutt (1998) relation is dependent on the models of Leitherer & Heckman (1995). These models were specifically created to correspond to the conditions that are prevalent within giant H II regions, H II galaxies, nuclear starbursts and IR luminous starburst galaxies, and traces diffuse gas within these regions. The Kennicutt (1998) relation assumes continuous starbursts of age 10–100 Myr, and requires the integrated IR luminosity over the range of 8–1000 μm.

The average Kennicutt SFR is $240 \pm 21\,\mathrm{M_\odot\ yr^{-1}}$ for the 'extended' and $223 \pm 25\,\mathrm{M_\odot\ yr^{-1}}$ for the 'classic' sample (Table 4); these values are consistent. Note that these estimates are determined from weighted stacking of the individual luminosities and SFRs derived from the 250 μm flux density of each galaxy rather than calculated from the weighted stacked flux density values in Table 2. The BAL and non-BAL average SFRs are also consistent within the errors. We find that the three detected BAL QSOs have SFR $> 1000\,\mathrm{M_\odot\ yr^{-1}}$. Since we cannot exclude the possibility that some fraction of the FIR emission comes from dust heated by the AGN, these SFRs should be regarded as upper limits. We also find that the average FIR luminosities presented in Table 4 for both the BAL and non-BAL QSO samples are, on their own, sufficiently large to classify them as ULIRGs. We note that the derived SFRs for each SPIRE band for IZw1 are more consistent than those determined for Mrk 231. This suggests that dust in BAL QSOs at higher z is likely cooler than that found in the low-z analogue Mrk 231. Finally, we have also investigated the effect of varying the dust temperature and β values and find that for plausible values ($25\mathrm{K} \le \mathrm{T} \le 60\,\mathrm{K}$ and $1.1 \le \beta \le 1.8$), there is about a factor of 2 variation in the final derived SFR values which does not change our conclusions.

4.4 FIR luminosity and C IV absorption-line equivalent width

From an analysis of submm wavelength data, Priddey et al. (2007) found a weak correlation between FIR flux density and C IV absorption-line equivalent width and a rather stronger statistical link between submm detection rate and C IV absorption-line equivalent width; i.e. of the 15 sources they observed, all six ($>2\sigma$) detections in the 850 μm band had a C IV absorption-line equivalent width of $\geq$25 Å. A KS test returned a probability of 0.01 that the detections and non-detections had the same C IV absorption-line equivalent width.

The small number of detections in our sample means that we cannot perform the same tests that Priddey et al. used. In our sample there are only five sources with C IV absorption-line equivalent

Table 4. The star formation rates and FIR luminosities of the detected (marked with an asterisk) BAL QSOs within the sample, along with the average star formation rate in the 250, 350 and 500 μm bandpasses and weighted mean for the 'extended', 'classic' and non-BAL samples as a whole using Mrk 231 and IZw1 as templates. We also include here our rare LoBAL QSO 115404.13+001419.6. We emphasize however that it is not reliably associated with $R > 0.80$ to a 250 μm source as with our detections and instead is the best estimate from measuring the flux density in the closest pixel of the PSF-smoothed map. At 500 μm it has a negative flux so SFRs are not included. The quoted $L_{\rm FIR}$ (using our ratio method for 250 μm) and SFR estimates are determined from weighted stacking of the individual luminosities and SFRs of each galaxy rather than calculated from the weighted stack values in Table 2 (shown in the flux density column), though the error will be underestimated as a result of confusion noise.

SDSS source	z	Flux density (250 μm) (mJy)	$\log_{10}(L_{\rm FIR}/L_\odot)$ (Mrk 231) (250 μm)	$\log_{10}(L_{\rm FIR}/L_\odot)$ (IZw1) (250 μm)	SFR ($M_\odot$ yr^{-1}) (Mrk 231)			SFR ($M_\odot$ yr^{-1}) (IZw1)			
					250	350	500	Mean	250	350	500	Mean
*085436.41+022023.5	1.9089	55.87 ± 6.81	12.87 ± 0.07	12.75 ± 0.10	1322 ± 199	2353 ± 364	3158 ± 754	1559 ± 175	1007 ± 227	1506 ± 343	1824 ± 532	1159 ± 189
*090517.24+013551.4	1.7678	57.81 ± 6.77	12.85 ± 0.06	12.71 ± 0.10	1248 ± 183	2386 ± 369	4092 ± 787	1473 ± 164	921 ± 204	1625 ± 357	2341 ± 597	1094 ± 177
*143907.51−010616.7	1.8214	73.35 ± 6.95	12.97 ± 0.06	12.84 ± 0.09	1640 ± 212	1535 ± 318	2297 ± 724	1608 ± 176	1224 ± 259	972 ± 269	1320 ± 471	1103 ± 187
115404.13+001419.6	1.6100	29.88 ± 6.65	12.51 ± 0.10	12.37 ± 0.13	580 ± 139	694 ± 250	–	607 ± 121	413 ± 121	427 ± 170	–	418 ± 99
'Extended' BAL QSO	–	11.81 ± 1.20	12.13 ± 0.04	11.92 ± 0.05	240 ± 21	297 ± 38	429 ± 94	253 ± 18	149 ± 17	151 ± 25	199 ± 56	150 ± 14
'Classic' BAL QSO	–	10.97 ± 1.51	12.10 ± 0.05	11.90 ± 0.06	223 ± 25	271 ± 44	336 ± 111	235 ± 22	141 ± 19	138 ± 29	154 ± 65	140 ± 16
Non-BAL QSO	–	10.94 ± 0.53	12.08 ± 0.02	11.84 ± 0.02	212 ± 8	293 ± 15	528 ± 36	230 ± 7	124 ± 6	148 ± 10	261 ± 22	130 ± 5

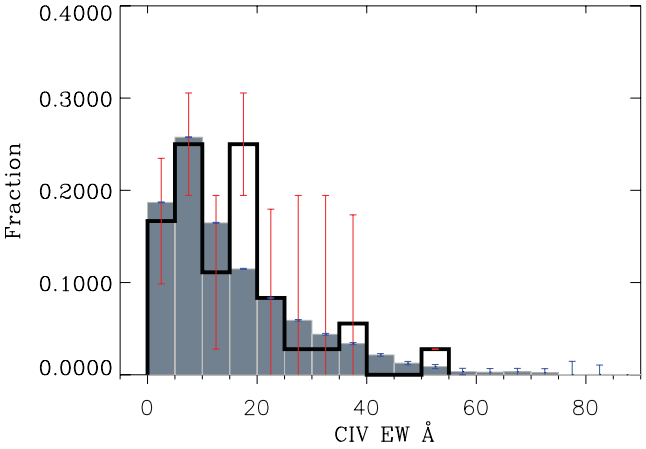

Figure 4. The distribution of C IV absorption-line equivalent width for the full Gibson et al. (2009a) sample (grey) and our 'classic' BAL QSO sample (black outline) in bins of width 5 Å. One source in the Gibson et al. (2009a) sample is omitted here, SDSS090901.80+535935.7, having a C IV absorption-line equivalent width of 193.9 Å. All others have C IV absorption-line equivalent widths below 90 Å.

widths of $\gtrsim$25 Å in the 250 μm bandpass, of which three are detections. Assuming a binomial probability distribution we estimate the probability of detections having C IV absorption-line equivalent widths $\gtrsim$25 Å by chance is only 0.005. However, these are detections in one bandpass alone and the number of objects with C IV absorption-line equivalent width $\gtrsim$25 Å is very small. We must therefore choose a different C IV absorption-line equivalent width cut-off for our HiBAL QSOs, such that we have similar sized samples to compare. We set this cut-off at $\geq$20 Å, which gives us 11 HiBAL QSOs to compare with the remaining 24 in the classic sample. For completeness we tested whether the distribution of C IV absorption-line equivalent widths within our restricted BAL QSO sample was representative of those within the parent population as described by Gibson et al. (2009a). A KS test on the C IV absorption-line equivalent widths of each population returns $p = 0.12$, so we are able to assume that our sample is representative. Fig. 4 shows histograms of the two C IV absorption-line equivalent width distributions. For this analysis we studied the 'classic' BAL QSO sample only since it suffers from less contamination from misclassified sources than the 'extended' sample due to the strictness of the BI mechanism. Furthermore, any true underlying physical relationship involving C IV absorption-line equivalent width will be expected to correlate with luminosity rather than flux density. We therefore determined the $L_{\rm FIR}$ luminosities of each BAL QSO using our assumed T and β for Mrk 231 and IZw1, separated them using our 20 Å cut-off and then performed a Mann–Whitney test (Mann & Whitney 1947) to determine whether a greater luminosity correlates with a larger C IV absorption-line equivalent width. For the Mrk 231 and IZw1 templates, respectively, the test returned probabilities of 0.23 and 0.22, which indicates that there is no significant evidence for a difference in the two subsamples. Obviously with this method there is the caveat that the BAL QSOs must each have a similar SED shape to our greybody templates but these results indicate there is no evidence for a dependence of FIR luminosity on C IV EW.

5 DISCUSSION

Our study shows that the FIR properties of HiBAL QSOs are statistically indistinguishable from those of non-BAL QSOs. We also

find that FIR emission has no dependence on C IV absorption-line equivalent width. Therefore, the FIR luminosity has no dependence on the absorption strength of the outflow, and our results do not require an evolutionary link between HiBAL and non-BAL QSOs. Rather a simple orientation effect argument is sufficient.

Priddey et al. (2007) found tentative evidence for a link between C IV absorption-line equivalent width and submm wavelength detection (albeit with a 2σ detection threshold). As discussed by Priddey et al. such a link could be used to argue that BAL QSOs are in a distinct evolutionary phase along the lines proposed by Page et al. (2004, 2011), where the QSO wind is in the process of terminating an epoch of enhanced star formation. Our results do not support this weak evidence for such a link between FIR output and C IV absorption-line equivalent width. The discrepancy may be linked to a possible selection effect discussed by Priddey et al. that the most reddened QSOs must be intrinsically more luminous to meet their blue selection criterion, and therefore the most extreme objects, which might host the most powerful outflows, would have higher dust reddening and higher FIR/submm output. This could explain why we see no such correlation, since the SDSS *i* band does not suffer reddening to as large a degree as the bluer bands in which past samples of QSOs were selected.

However, a caveat to our results is that our sample is composed almost entirely of HiBAL QSOs. We have not considered either LoBAL QSOs or their rarer FeLoBAL cousins, which may well show FIR properties inconsistent with a simple orientation scheme hypothesis (see below). We note that the samples of Willott et al. (2003) and Priddey et al. (2007) were also mostly composed of HiBAL QSOs. The Priddey et al. (2007) sample contains only one known LoBAL QSO, and many of the Willott et al. (2003) QSOs classified as LoBAL QSOs are uncertain due to Mg II moving out of the spectral range at $z > 2.26$.

Regarding studies at other wavelengths, the findings of Green et al. (2001) carried out using the *Chandra X-ray Observatory* provide weak evidence that HiBAL QSOs appear X-ray weak due to intrinsic absorption, and that their underlying emission is actually the same as that of non-BAL QSOs (Gallagher et al. 2002, 2006; Gibson et al. 2009b), which supports an orientation scheme. In contrast, even taking into account intrinsic absorption, LoBAL QSOs remain X-ray weak. An analysis of X-ray absorption performed by Streblyanska et al. (2010) suggests that LoBALs and HiBALs may be physically different objects. This is reinforced by composite SEDs ranging from X-ray to radio generated by Gallagher et al. (2007) who find similarities between the SEDs of HiBALs and non-BAL QSO but differences between these populations and LoBALs. However, it should be noted that the absorbed nature of BAL QSOs means that their X-ray data are limited in quality, so these findings cannot be taken as conclusive.

Certainly LoBAL QSOs are found to have redder spectra than other types (Reichard et al. 2003b), implying a larger dust mass in the host galaxy and/or vicinity of the supermassive black hole (SMBH). The idea that LoBALs and FeLoBALs form a separate evolutionary class finds support from the work of Farrah et al. (2007) and Urrutia et al. (2009). Farrah et al. (2007) argue that FeLoBAL QSOs are galaxies where a massive merger driven starburst is ending, and the last remnants of a dust cocoon are being removed by a rapidly accreting SMBH at the galaxy's centre. The SED fits of those detected at longer wavelengths (4/9) require a starburst component of the order of several hundred solar masses per year, which is taken to imply that FeLoBAL QSOs are associated with ULIRGs. Similar conclusions are drawn in Farrah et al. (2010) who find that FeLoBAL QSOs span a range of spectral shapes, consistent with the idea that they may be a transition phase in the lifetime of an AGN. However, as noted in their papers, the small and inhomogeneous sample sizes render such conclusions tentative. A larger sample was presented by Farrah et al. (2012) of 31 objects with optical to FIR photometry. These were found to all be highly luminous ($>10^{12}\,L_{\odot}$), yet the bulk of IR emission in the majority of sources came from the AGN rather than a starburst component. The mid-IR and FIR properties of the FeLoBAL QSOs spanning the redshift range $0.8 < z < 1.8$ presented by Farrah et al. further reinforce the idea that they are a class apart from the general QSO population.

Urrutia et al. (2009) also found an unusually high percentage (32 per cent using the conservative BI selection) of LoBAL QSOs in a sample of dust reddened type 1 QSOs; in fact, all of these objects can also be classified as FeLoBALs. The orientation hypothesis is irreconcilable with such findings allowing an evolutionary hypothesis to be invoked, even with the caveats offered by Urrutia et al. (2009).

The subset of the full Gibson et al. (2009a) sample studied here contains only one QSO, SDSS115404.13 + 001419.6, classified as a LoBAL. These objects are rare, making up only 15 per cent of all observed BAL QSOs. A very deep C IV absorption trough (greater than anything seen in the HiBAL sample), combined with a high flux density (29.88 ± 6.65 mJy at 250 μm), makes it a conspicuous member of our sample. However, little can be said of an entire population from one object. Future work in the FIR/submm wavebands targeting LoBALs and/or FeLoBALs would be invaluable.

6 CONCLUSIONS

(i) Using a stacking analysis we have determined that HiBAL QSOs at $1.5 \leq z < 2.3$ are statistically indistinguishable in terms of FIR luminosity (and therefore SFR) from a matched sample of non-BAL QSOs. This result is broadly consistent with previous work conducted at submm wavelengths (Willott et al. 2003; Priddey et al. 2007). The average FIR luminosities of both our HiBAL and non-BAL samples are $\gtrsim 10^{12}\,L_{\odot}$, sufficient to classify them as ULIRGs. We calculate weighted mean SFRs (strictly upper limits using this relation due to the possibility of dust heating by the AGN and our BAL QSOs having overdensities of neighbours) for the HiBALs of $240 \pm 21\,M_{\odot}\,yr^{-1}$ for the 'extended' and $223 \pm 25\,M_{\odot}\,yr^{-1}$ for the 'classic' sample from the flux density at 250 μm.

(ii) While Priddey et al. (2007) found tentative evidence for a dependence of submm flux density on C IV absorption-line equivalent width, we find no such dependence at FIR wavelengths. We suggest that the Priddey et al. result may have been due to small number statistics and selection effects as noted in the discussion.

(iii) Within our samples, 3/49 HiBALs and 27/329 non-BALs are detected at $>5\sigma$ significance. The detection rates for the two species are statistically indistinguishable.

(iv) Taken together these results suggest that BALs (strictly HiBALs) can be unified with non-BAL QSOs within a simple orientation scheme where a BAL QSO is observed only if a nuclear outflow intercepts our line of sight. However, with the current data we are unable to say whether (Fe)LoBALs can similarly be accommodated within this scheme or whether they form a distinct population perhaps caught at a key phase in their evolution. Future observations at FIR/submm wavelengths would be valuable in this respect.

ACKNOWLEDGMENTS

JMCO would like to thank STFC for a studentship and we thank the anonymous referee for useful comments that have improved the paper.

The *Herschel*-ATLAS is a project with *Herschel*, which is an ESA space observatory with science instruments provided by European-led Principal Investigator consortia and with important participation from NASA. The H-ATLAS website is http://www.h-atlas.org/.

This research has made use of the NASA/IPAC Extragalactic Database (NED) which is operated by the Jet Propulsion Laboratory, California Institute of Technology, under contract with the National Aeronautics and Space Administration.

REFERENCES

Antonucci R., 1993, ARA&A, 31, 473
Arav N. et al., 2001, ApJ, 561, 118
Bavouzet N., 2008, PhD thesis, Univ. Paris Sud 11
Best P. N., 2007, New Astron. Rev., 51, 168
Best P. N., Heckman T. M., 2012, MNRAS, 421, 1569
Béthermin M., Dole H., Beelen A., Aussel H., 2010, A&A, 512, A78
Bonfield D. G. et al., 2011, MNRAS, 416, 13
Booth C. M., Schaye J., 2009, MNRAS, 398, 53
Bower R. G., Benson A. J., Malbon R., Helly J. C., Frenk C. S., Baugh C. M., Cole S., Lacey C. G., 2006, MNRAS, 370, 645
Brotherton M. S., Tran H. D., Becker R. H., Gregg M. D., Laurent-Muehleisen S. A., White R. L., 2001, ApJ, 546, 775
Carilli C. L. et al., 2001, ApJ, 555, 625
Churchill C. W., Schneider D. P., Schmidt M., Gunn J. E., 1999, AJ, 117, 2573
Cirasuolo M., McLure R. J., Dunlop J. S., Almaini O., Foucaud S., Simpson C., 2010, MNRAS, 401, 1166
Cowie L. L., Songaila A., Hu, Cohen J. G., 1996, AJ, 112, 839
Croton D. J. et al., 2006, MNRAS, 365, 11
Dai X., Shankar F., Sivakoff G. R., 2008, AJ, 672, 108
De Lucia G., Blaizot J., 2007, MNRAS, 375, 2
DiPompeo M. A., Brotherton M. S., Becker R. H., Tran H. D., Gregg M. D., White R. L., Laurent-Muehleisen S. A., 2010, ApJS, 189, 83
DiPompeo M. A., Brotherton M. S., De Breuck C., Laurent-Muehleisen S. A., 2011, ApJ, 743, 71
Eales S. et al., 2010, PASP, 122, 499
Elvis M., 2000, ApJ, 545, 63
Elvis M. et al., 1994, ApJS, 95, 1
Farrah D., Lacy M., Priddey R., Borys C., Afonso J., 2007, ApJ, 662, L59
Farrah D. et al., 2010, ApJ, 717, 868
Farrah D. et al., 2012, ApJ, 745, 178
Gabel J. R., Arav N., Kim T., 2006, ApJ, 646, 742
Gallagher S. C., Brandt W. N., Chartas G., Garmire G. P., 2002, ApJ, 567, 37
Gallagher S. C., Brandt W. N., Chartas G., Priddey R., Garmire G. P., Sambruna R. M., 2006, ApJ, 644, 709
Gallagher S. C., Hines D. C., Blaylock M., Priddey R. S., Brandt W. N., Egami E. E., 2007, ApJ, 665, 157
Gibson R. R. et al., 2009a, ApJ, 692, 758
Gibson R. R., Brandt W. N., Gallagher S. C., Schneider D. P., 2009b, ApJ, 696, 924
Granato G. L., De Zotti G., Silva L., Bressan A., Danese L., 2004, ApJ, 600, 580
Green P. J., Alcroft T. L., Mathur S., Wilkes B. J., Elvis M., 2001, ApJ, 558, 109
Griffin M. J. et al., 2010, A&A, 518, L3
Hall P. B. et al., 2002, ApJS, 141, 267
Hamann F., Ferland G., 1999, ARA&A, 37, 487
Hamann F., Barlow T., Cohen R. D., Junkkarinen V., Burbidge E. M., 1997, in Arav N., Shlosman I., Weymann R. J., eds, ASP Conf. Ser. Vol. 128, Mass Ejection from Active Galactic Nuclei, Astron. Soc. Pac., San Francisco, p. 19
Hardcastle M. J. et al., 2010, MNRAS, 409, 122
Hatziminaoglou E. et al., 2010, A&A, 518, L33
Hewett P. C., Foltz C. B., 2003, AJ, 125, 784
Ho L. C., Kim M., 2009, ApJS, 184, 398
Ibar E. et al., 2010, MNRAS, 409, 38
Kennicutt R. C., Jr, 1998, ARA&A, 36, 189
Lazarova M. S., Canalizo G., Lacy M., Sajina A., 2012, ApJ, 755, 29
Leitherer C., Heckman T. M., 1995, ApJS, 96, 9
Lewis G. F., Chapman S. C., Kuncic Z., 2003, ApJ, 596, L35
McCarthy I. G. et al., 2010, MNRAS, 406, 822
Mann H. B., Whitney D. R., 1947, Ann. Math. Stat., 18, 50
Murray N., Chang J., 1998, ApJ, 494, 125
Murray N., Chang J., Grossman S. A., Voit G. M., 1995, ApJ, 451, 498
Ogle P. M., Cohen M. H., Miller J. S., Tran H. D., Goodrich R. W., Martel A. R., 1999, ApJS, 125, 1
Omont A., McMahon R. G., Cox P., Kreysa E., Bergeron J., Pajot F., Storrie-Lombardi L. J., 1996, A&A, 315, 1
Page M. J., Stevens J. A., Ivison R. J., Carrera F. J., 2004, ApJ, 611, L85
Page M. J., Carrera F. J., Stevens J. A., Ebrero J., Blustin A. J., 2011, MNRAS, 416, 2792
Pascale E. et al., 2011, MNRAS, 415, 911
Peacock J. A., 1983, MNRAS, 202, 615
Pilbratt G. L. et al., 2010, A&A, 518, L1
Poglitsch A. et al., 2010, A&A, 518, L2
Priddey R. S., Isaak K. G., McMahon R. G., Omont A., 2003, MNRAS, 339, 1183
Priddey R. S., Gallagher S. C., Isaak K. G., Sharp R. G., McMahon R. G., Butner H. M., 2007, MNRAS, 374, 867
Rawlings S., Jarvis M. J., 2004, MNRAS, 355, L9
Reichard T. A. et al., 2003a, AJ, 125, 1711
Reichard T. A. et al., 2003b, AJ, 126, 2594
Rigby E. E. et al., 2011, MNRAS, 415, 2336
Sanders D. B., Mazzarella J. M., Kim D.C, Surace J. A., Soifer B. T., 2003, AJ, 126, 1607
Scannapieco E., Silk J., Bouwens R., 2005, ApJ, 635, L13
Scaringi S., Cottis C. E., Knigge C., Goad M. R., 2009, MNRAS, 399, 2231
Schneider D. P. et al., 2005, AJ, 130, 367
Schneider D. P. et al., 2007, AJ, 134, 102
Sijacki D., Springel V., Di Matteo T., Hernquist L., 2007, MNRAS, 380, 877
Smith P. S., Schmidt G. D., Allen R. G., Angel J. R. P., 1995, ApJ, 444, 146
Smith D. J. B. et al., 2011, MNRAS, 416, 857
Sprayberry D., Foltz C. B., 1992, ApJ, 390, 39
Springel V., Di Matteo T., Hernquist L., 2005, ApJ, 620, L79
Streblyanska A., Barcons X., Carrera F. J., Gil-Merino R., 2010, A&A, 515, 2
Tolea A., Krolik J. H., Tsvetanov Z., 2002, ApJ, 578, L31
Trump J. R. et al., 2006, ApJS, 165, 1
Urrutia T., Becker R. H., White R. L., Glikman E., Lacy M., Hodge J., Gregg M. D., 2009, ApJ, 698, 1095
Voit G. M., Weymann R. J., Korista K.T, 1993, ApJ, 413, 95
Weymann R. J., Morris S. L., Foltz C. B., Hewett P. C., 1991, ApJ, 373, 23
Willott C. J., Rawlings S., Grimes J. A., 2003, ApJ, 598, 909

This paper has been typeset from a TEX/LATEX file prepared by the author.